IGS

Article

Black carbon effects and seasonal isotope records in the Godwin-Austen snowpack and K2 high-altitude camps

Nicolás González-Santacruz[1] , Francisco Fernandoy[2], Kumiko Goto-Azuma[3] , Motohiro Hirabayashi[3], Raul R. Cordero[4], Sarah Feron[4,5] and Sérgio Henrique Faria[1,6]

[1]Basque Centre for Climate Change (BC3), Leioa, Spain; [2]Laboratorio de Análisis Isotópico, Universidad Andrés Bello, Viña del Mar, Chile; [3]National Institute of Polar Research, Tachikawa, Tokyo, Japan; [4]Universidad de Santiago de Chile, Santiago, Chile; [5]University of Groningen, Leeuwarden, The Netherlands and [6]IKERBASQUE, Basque Foundation for Science, Bilbao, Spain

Abstract

This study investigates black carbon (BC) concentrations in the seasonal snowpack on the Godwin-Austen Glacier and in surface snow at K2 Camps 1 and 2 (Karakoram Range), assessing their impact on snowmelt during the 2019 ablation season. Potential BC and moisture sources were identified through back-trajectory analysis and atmospheric reanalyses. Variations in water stable isotopes ($\delta^{18}O$ and δ^2H) in the snowpack were analysed to confirm its representativeness as a climatic record for the 2018–19 accumulation season. The average BC concentration in the snow pits (12 ng g^{-1}) generated 66 mm w.e. (or 53 mm w.e. excluding the basal zone) of meltwater. Surface snow at K2 Camp 1 showed BC concentrations of 7 ng g^{-1}, consistent with those on the snowpack surface, suggesting it may reflect local BC levels in late February 2019. In contrast, higher concentrations at K2 Camp 2 (26 ng g^{-1}) were potentially linked to expedition activities.

1. Introduction

The High Mountain Asia (HMA) region covers an area of 3.8 million km^2 (Baumann and others, 2009) and encompasses parts of Afghanistan, Pakistan, India, Nepal, China, Tibet, Bhutan, Kazakhstan, Uzbekistan, Kyrgyzstan and Tajikistan. This region is also known as the 'third pole' due to hosting the largest concentration of ice outside the polar regions (IPCC, 2013). Here lie the headwaters of some of the major rivers of the Asian continent, such as the Indus, Ganges, Brahmaputra, Yangtze and Yellow (Pritchard and others, 2019). Collectively, these hydrographic basins provide water to more than a billion people, constituting over 20% of the global population (GPWv3, 2005; Immerzeel and others, 2010, 2020; IPCC, 2013).

The meltwater generated by the glaciers and snow cover in HMA plays a critical role in safeguarding this vast population from severe water scarcity during summer or droughts. The additional flow integrates into the river systems, offsetting the decrease in discharge resulting from the reduced rainfall amount and frequency. Each summer, the volume of meltwater produced in HMA is ∼36 km^3, increasing to 37 km^3 in drought years (Pritchard and others, 2019). This buffering effect is more pronounced in the most glacierized areas of HMA (i.e., the Hindu-Kush, Karakoram and Himalayan ranges) which house extensive valley glaciers. Therefore, the contributions of glacial meltwater to the rivers are indispensable for sustaining services such as water supply, agricultural irrigation and hydropower generation.

Unfortunately, HMA cryosphere has shown degradation signals since the mid-19th century (Bolch and others, 2012), a situation that has become aggravated in the 21st century, as reflected in some studies conducted in the last two decades (e.g., IPCC, 2019; Zemp and others, 2019). This loss of critical glacier mass will inevitably lead to a long-term decrease in glacier-derived meltwater runoff. In the past century, droughts were the most devastating natural disasters in the region, resulting in ∼6 million deaths and affecting ∼1.1 billion people (National Research Council, 2012). Moreover, reduction in food production due to water deficit can lead to social instability, sudden and uncontrolled migrations and intra- and interstate conflicts (World Economic Forum, 2016).

One of the degradation factors is the emission of black carbon (BC) into the atmosphere, an aerosol with a high carbon content that can be generated by human activities through the incomplete combustion of fossil fuels or biomass burning (Bond and others, 2013). The residence time of these BC particles is typically ∼1 week (Ramanathan and Carmichael, 2008; Lee and others, 2013), facilitating their dispersion over distances that can exceed 1000 km (Rodhe and others, 1972; Bond and others, 2013). The HMA

region is surrounded by important global BC emitting centres like East, Southeast and South Asia, with countries like China and India standing out (Lu and others, 2012; Bond and others, 2013; IPCC, 2013). When BC particles are deposited on the snow or ice surface, they tend to absorb a higher proportion of shortwave solar irradiance, reducing the surface albedo, warming the particles and eventually increasing the melting rate of the snow (e.g., Flanner and others, 2007; Ménégoz and others, 2014) and ice (e.g., Xu and others, 2009a, 2009b; Kaspari and others, 2011). Therefore, due to its geographical context, HMA is one of the most vulnerable regions in the world to the effects of BC.

This study examines the impact of BC on snowmelt during the 2019 ablation season. Samples were collected from two snow pits excavated in the seasonal snowpack on the Godwin-Austen Glacier, as well as from surface snow at K2 Camps 1 and 2. To provide additional context, measurements of water stable isotopes (δ^{18}O and δ^2H) were used to evaluate the representativeness of the snowpack as a record for the 2018–19 accumulation season, enhancing interpretations of likely BC and moisture sources and the timing of BC deposition.

2. Study framework

The Godwin-Austen Glacier in the Central Karakoram is part of the Upper Indus Basin (UIB; Fig. 1a). This basin has an extensive glaciated area, covering ~22 000 km^2 (Immerzeel and others, 2010) and faces dry summers and moderately wet winters. Approximately 49% of the annual precipitation falls as snow (Pritchard and others, 2019) that covers ~85% of the basin area in winter (Shrestha and others, 2015). Various studies have reported that more than half of the annual Indus River flow comes from the snowpack (seasonal or perennial) and glacier melting (e.g., Hewitt and others, 1989; Wake, 1989; Young and Hewitt, 1990; Archer and Fowler, 2004; Bookhagen and Burbank, 2010). Particularly noteworthy is the contribution of seasonal snowpacks, as highlighted by the study of Yu and others (2013), which indicated that the meltwater of the glaciers located in the Karakoram, western Himalayas and Hindu-Kush contributes ~18% of the total flow in the Indus basin, while the remaining 82% comes from the melting of seasonal snowpacks. In this context, the net annual volume of meltwater in the Indus River over the 4 month ablation season is 14.5 ± 3.1 km^3 (Pritchard and others, 2019). The meltwater produced counteracts the reduction of river discharge caused by decreased precipitation during the thawing season or drought, making it a crucial resource. This is especially important considering that the economy of the Indus River lowlands, highly dependent on agriculture (Bhatti and others, 2009), relies on the largest network of irrigation channels in the world, the IBIS (Indus Basin Irrigation System). The IBIS can extract up to 75% of the Indus River flow, making this basin one of the most depleted worldwide (Sharma and others, 2010).

3. Methods

Between January and February 2019, we stayed at K2 Base Camp (K2BC; 5150 m a.s.l.), located on the western moraine of the Godwin-Austen Glacier (Fig. 1b and c). We excavated two snow pits on the glacier, selecting sites far from K2BC to minimize contamination from emissions. Based on the automatic weather station (AWS) data indicating prevailing west-to-east winds, we chose locations south of K2BC. Snow pit 1 (P1; 35°49.486' N, 76°30.779' E; 4937 m a.s.l.) was located 950 m south of K2BC and reached a depth of 120 cm, while Snow pit 2 (P2; 35°49.184' N,

76°30.920' E; 4927 m a.s.l.) was 500 m further south, reaching a depth of 200 cm (Fig. 1c). Both snow pits covered the full snowpack thickness (Fig. S1). Additionally, mountaineers collected surface snow samples at K2 Camp 1 (6076 m a.s.l.; 35°51.95' N, 76°32.17' E) and Camp 2 (6650 m a.s.l.; 35°52.15' N; 76°31.99' E).

3.1. In situ measurements and sampling

The snow pits were excavated in late February 2019, with P1 on 24 February 2019 and P2 on 27 February 2019. Works in P1 started at 10:56 UT (UTC + 5) and took ~3 h, while P2 began at 11:50 UT (UTC + 5) and took around 5 h due to its greater depth. Snow temperature and density were measured at intervals of 5 and 8 cm, respectively, using a TFA® digital thermometer with a precision of ± 0.5 °C, and a 125.5 cm^3 box cutter based on the original design of the Institute of Low Temperature Science of the Hokkaido University. Snow samples for BC measurements and stable isotopes were collected at 6–8 cm intervals, with volumes of 1300–1800 cm^3, stored in Whirlpack™ bags and melted at room temperature (~10ºC). The melted samples were homogenized, transferred into 30 mL glass vials and kept at 1–5°C during shipping, as plastic bottles can alter isotopic signals during long-term storage (Spangenberg and Vennemann, 2008; Spangenberg, 2012).

3.2. Chemical analysis

The National Institute of Polar Research in Tokyo, Japan, performed the chemical analysis of the water samples. For BC measurements, a modified Single-Particle Soot Photometer (SP2; Droplet Measurement Technologies, Longmont, CO, USA) was used, employing the Laser-Induced Incandescence method to measure BC based on its refractory properties (e.g., Kaspari, 2011; Sterle and others, 2013). The advantages of the SP2 include its lack of requirement for prior water sample filtering, low water volume requirements, the possibility of using a continuous flow system and it is not sensitive to other materials, avoiding potential sources of uncertainty associated with filtration methods. In this particular case, we used a Wide-Range Single-Particle Soot Photometer (Mori and others, 2016), a modified version of the standard SP2 with a high-efficiency nebulizer (Marin-5, CETAC Technologies Inc., Omaha, NE, USA). This combination allows to measure BC particles with diameters between 70 and 4000 nm, whereas a standard SP2 would only allow us to measure BC particles with diameters between ~70 and 500 nm.

Complementing the BC analysis, water stable isotopes (^{18}O and ^{2}H, or deuterium) were measured using an Isotopic Ratio Mass Spectrometer, with a precision of ± 0.5‰ to ± 0.6‰ for δD and ± 0.01‰ to ± 0.11‰ for δ^{18}O (Uemura and others, 2007). Isotopic data are particularly useful, as the δ^{18}O content in precipitation reflects atmospheric condensation temperatures, with colder conditions leading to lower δ^{18}O values, which can be preserved in the snowpack (Dansgaard, 1964; Friedman and others, 1992; Mayer and others, 2014). Additionally, δ^2H and δ^{18}O follow a global linear correlation known as the Global Meteoric Water Line (GMWL), with the y-axis intercept (10‰) referred to as deuterium excess or d-excess (Epstein and Mayeda, 1953; Friedman, 1953; Craig, 1961; Dansgaard, 1964). Variations in atmospheric humidity during evaporation modify the GMWL and, consequently, the d-excess. Higher humidity at the source results in lower d-excess values, and vice versa, helping to identify moisture sources and trace the origin of water vapour (Jouzel, 1982; Rindsberger and
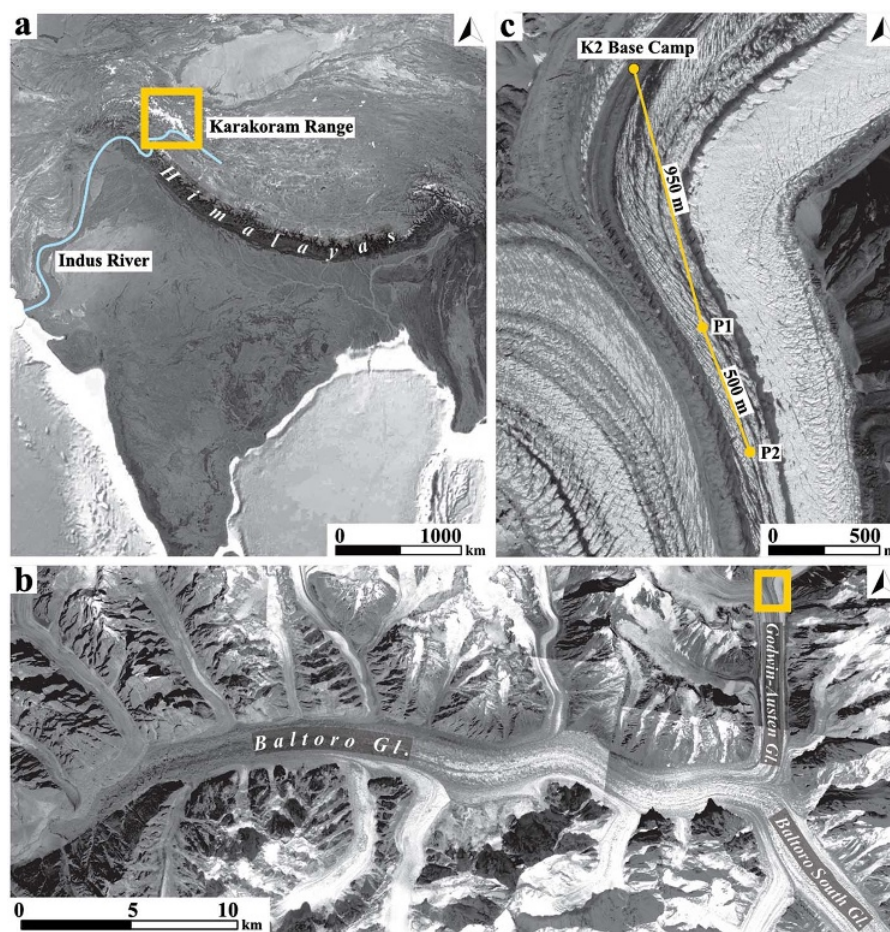
Figure 1. (a) Geographical context of the Karakoram range (yellow square) and Indus river (light blue line). (b) The yellow rectangle indicates the study area within the glacier system composed of the Baltoro Glacier, Godwin-Austen Glacier and Baltoro South Glacier. (c) Position of the snow pits (P1 and P2) relative to the K2 Base Camp.

others, 1983; Pfahl and Sodemann, 2014; Galewsky and others, 2016).

3.3. Atmospheric reanalyses

For this study, it was essential to have meteorological records (e.g., temperature, precipitation, solar irradiance, cloud cover) from the Godwin-Austen Glacier during the winter of 2018–19 and the 2019 ablation season. To obtain that information, an AWS was set up at K2BC during the expedition (January 2018–March 2019), providing highly accurate data on temperature and wind speed and direction. Unfortunately, due to technical issues, the data were only available from 3 February onwards. Moreover, meteorological variables like temperature and precipitation vary significantly with elevation, and data tend to be biased because stations are typically located in valley bottoms (Wake, 1989). For instance, on the K2 southern slope, precipitation ranges from 150 to 200 mm a^{-1} in the elevation range 2000–3200 m a.s.l., with values of 1600 at 6100 m a.s.l., and reaching 2500 mm a^{-1} at 8000 m a.s.l. (Decheng, 1978; Mayer and others, 2006). Consequently, we resorted to atmospheric reanalysis to obtain continuous meteorological data, specifically ERA5 (Hersbach, 2016), as validated for the UIB by studies from Dahri and others (2021) and Baudouin and others (2020). For regional atmospheric BC concentrations, we used NASA's MERRA-2 data from the Global Modeling and Assimilation Office.

3.4. Back-trajectory analysis

To analyse the snowpack isotopic data and BC content from a global and regional atmospheric circulation perspective, we employed the Hybrid Single-Particle Lagrangian Integrated Trajectory model (HYSPLIT; Stein and others, 2015; Rolph and others, 2017). This model calculates daily back-trajectories of air parcels before reaching the Godwin-Austen Glacier. For meteorological data, we used the Global Data Assimilation System, developed by NOAA in conjunction with the National Centers for Environmental Prediction (NCEP), with a 0.5° × 0.5° latitude/longitude resolution. From the start of the accumulation season in October 2018 (Archer and Fowler, 2004; Hasson and others, 2016) to the snow pit excavation on 24–27 February, we computed 180 back-trajectories at two altitudes (500 and 1500 m above ground level, a.g.l.) to capture variations in air mass origins across different heights, using the snow pits as endpoints. To simplify the analysis, we grouped the trajectories by month using Total Spatial Variance and the K-means clustering algorithm (Fig. S2; Hartigan and Wong, 1979; NOAA, 2023a; NOAA, 2023b). Notably, different algorithms may yield variations in results, even when applied to the same dataset (Cui and others, 2021). These clusters help identify probable regional BC emission sources, the origins of predominant air masses and potential moisture sources contributing to snowpack formation (Sinclair and Marshall, 2009).

Back-trajectories were classified considering the last major water body that air parcels passed over before reaching the study site. Although moisture gains and losses could occur along their

path, the isotopic signature of the precipitation is likely predominantly influenced by the moisture from these large water bodies. Using this criterion, we established six domains: one circular (Domain 1) and five wedge-shaped (or radial; Domain 2–6), using snow pits coordinates as reference points (see Figure 4). Each radial domain consists of two regions based on the distance to the study site. This division is similar to the one proposed by Juhlke and others (2019) for the Pamir Mountains, based on the relative humidity data provided by HYSPLIT. Domain 1 is centred on the snow pits and covers a radius of ∼500 km, whereas the wedge-shaped domains are North Central Asia and Siberia (Domain 2), the Caspian Sea and Black Sea (Domain 3), the Middle East and Mediterranean Sea (Domain 4), the Persian Gulf and Red Sea (Domain 5) and Northern India and the Arabian Sea (Domain 6).

3.5. Albedo reduction, radiative forcing and snowmelt

To assess the impact of BC, we needed to determine the span of the 2019 ablation season in the Godwin-Austen glacier region. The removal of the K2BC weather station in early March 2019 left us without direct temperature data, so we relied on previous studies. On the one hand, our field observations in late February showed no signs of liquid water or refreezing layers, indicating the snowpack was still 'dry' at that time. On the other hand, studies by Lund and others (2020), Ahmad and others (2020), Mukhopadhyay and others (2015) and Yi and others (2021) indicate that snowmelt in the Karakoram generally spans from May to September. Consequently, this is an extrapolation from previous research rather than direct in situ data.

For estimating the effects of BC on snow albedo reduction, radiative forcing and melt rates, we used parameterizations by Dang and others (2015, 2017), which account for BC particle concentration, shortwave solar irradiance, average snowpack ice crystal size (Flanner and others, 2007) and cloud fraction (CF; Dang and others, 2017). This method can only be applied to 'semi-infinite' snowpacks, thick enough to hide the underlying surface for all wavelengths (Dang and others, 2015), and has been already used in the Andes and Antarctic Peninsula (Cordero and others, 2022a, 2022b).

We calculated the albedo reduction (ΔA) under two atmospheric conditions: clear sky (ΔA_{clear}) and cloudy sky (ΔA_{cloudy}). The parameterizations consider the combined effect of BC particles and snow crystal size variation on ΔA. A given concentration (C) of BC in a snowpack with an average snow crystal radius (r) can produce an ΔA similar to those in a snowpack with lower BC concentrations and larger average radius. For instance, snow with a BC concentration of 20 ng g^{-1} and an average snow crystal radius of 100 μm reduces albedo by 0.5%, whereas if the radius is 1000 μm (and equal BC concentration), the albedo is reduced by 1.6% (Dang and others, 2015). In the infrared spectrum, snow albedo is primarily controlled by the size and shape of ice crystals (Wiscombe and Warren, 1980; Warren, 1982). On the other hand, in the visible spectrum, albedo is more influenced by particles with high carbon content (e.g., BC), which increase photon absorption, thereby decreasing the reflective capacity of the snow (i.e., lower albedo; Chýlek and others, 1995).

As proposed by Dang and others (2015), the r and C variables can be combined to calculate ΔA through the definition of the following parameter:

$$H = \left(\frac{C}{C_0}\right)\left(\frac{r}{r_0}\right)^s,$$

where C_0 is a BC reference concentration (10^{-6} ng g^{-1}) and r_0 is a reference crystal radius (100 μm). The exponent s takes the value 0.73 (Table 3 in Dang and others, 2015). The albedo reduction (ΔA) is related to H by a quadratic function:

$$\log_{10}\left(\Delta A\right) = m_1 \cdot p^2 + m_2 \cdot p + m_3,$$

where

$$p = \log_{10}H.$$

The coefficients m_1, m_2 and m_3 are defined in Table 3 of Dang and others (2015) for both clear sky and cloudy conditions; therefore, we can compute the parameters ΔA_{clear} and ΔA_{cloudy}. It is important to note that these calculations are only valid for crystal radii ranging from 50 to 2500 μm. According to Dang and others (2017), the total albedo reduction (ΔA) can be estimated by

$$\Delta A = CF \cdot \Delta A_{\text{cloudy}} + (1 - CF) \cdot \Delta A_{\text{clear}},$$

where CF represents the average cloud fraction over the melting season, ranging between 0 and 1, with 0 indicating the complete absence of clouds and 1 denoting full coverage. The radiative forcing of BC (RF_{BC}) is computed by multiplying the total albedo reduction (ΔA) by the average incoming solar irradiance or shortwave irradiance (I):

$$RF_{\text{BC}} = \Delta A \cdot I.$$

The values of CF and I are derived from the ERA5 atmospheric reanalysis (Hersbach, 2016). The RF_{BC} is a product of an increased absorption of solar irradiance by BC particles, resulting in snowpack surface warming. This extra energy absorbed per unit surface of the snowpack (E_x) can be calculated by multiplying RF_{BC} by the duration of the melting season (d):

$$E_x = RF_{\text{BC}}d.$$

Finally, we calculate W, which is the snow that melts sooner due to RF_{BC}:

$$W = \frac{\Delta A \cdot I \cdot d}{E},$$

where E represents the water latent heat of fusion (Cohen, 1994).

4. Results

4.1. Temperature and mass density

Both snow pits (P1 and P2) showed similar temperature variations despite differences in depth (121 cm in P1 and 200 cm in P2). Near the surface (top 10 cm), temperature differences were minimal with −13.7°C in P1 and −13.5°C in P2, whereas the bottom showed a temperature of −9.5°C in P1 and −9.1°C in P2. A pronounced temperature decrease occurred in the upper layers, with a gradient of −0.32°C cm^{-1} in P1 and −0.26°C cm^{-1} in P2, reaching lows of −16.7°C at 10 cm in P1 and −18.8°C at 20 cm in P2. Below these points, temperatures decreased gradually at a rate of 0.065°C cm^{-1} in P1 and 0.053°C cm^{-1} in P2 down to the snowpack base (Fig. S3).

Average mass density was 292 kg m^{-3} in P1 and 333 kg m^{-3} in P2, with lower densities in the surface layers (211 kg m^{-3}), some layers in the central section (249 kg m^{-3}) and at the snow–ice interface (289 kg m^{-3}). The low-density surface layer had
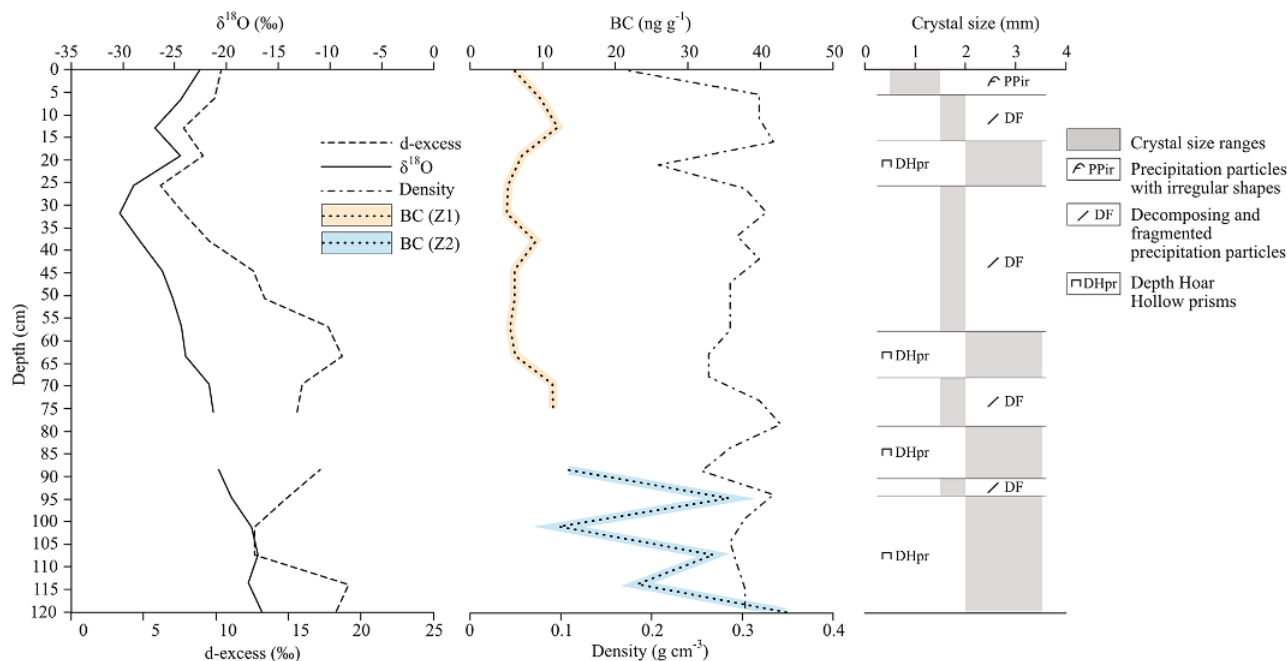
Figure 2. Measurements along P1. (Left) Isotopic variations with $\delta^{18}O$ (top) and d-excess (bottom). (Centre) variation in black carbon (BC) concentrations (top) with differentiation between zones Z1 (orange) and Z2 (blue), along with mass density fluctuations (bottom). (Right) Evolution of grain size range with depth and grain shape classification according to Colbeck (1990) and Fierz and others (2009).

crystal sizes ranging from <1.0 to 1.5 mm and exhibited irregular and rounded shapes. In contrast, the low-density layers in the central and basal sections had larger crystals (2.0–3.5 mm) characterized by well-defined faces and edges. Although the P2 basal low-density layer was thicker compared to P1, the crystals in P1 were slightly larger and faceted. Sampling the intermediate and basal low-density layers was quite challenging, as crystals tended to disintegrate due to low cohesion. In the remaining snowpack, the ice crystals ranged between 1.5 and 2.0 mm (Figs. 2 and 3).

4.2. Isotopic variations

Samples were collected at 6 cm intervals along P1 and 8 cm intervals along P2, with the average isotopic values assigned to the midpoints of the sampling intervals. Despite some data gaps, the resolution was adequate to establish correlations between the snow pits.

The $\delta^{18}O$ had a similar trend in both snow pits. At the surface, the values were −22.2‰ for P1 and −21.7‰ for P2. As depth increased, we observed a gradual depletion of isotope values, reaching the minimum at 33 cm in P1 (−30.4‰) and at 75 cm in P2 (−30.5‰). From this point, $\delta^{18}O$ in P1 increased until reaching the maximum enrichment (−16.3‰) at 108 cm and then descended to −16.5‰ at the snowpack base. The second snow pit (P2) reached its less depleted value (−17.8‰) at 192 cm before reaching the ice contact with a value of −18.5‰. Regarding d-excess, the values at the surface were also comparable: 10.2‰ in P1 and 10.5‰ in P2. As depth increased, d-excess decreases until reaching its minimum values of 6.1‰ in P1 at 27 cm depth and 4.4‰ in P2 at 68 cm depth. With further depth increase, values progressively rose, peaking at 18.6‰ at 63 cm in P1 and 18‰ at 140 cm in P2. Towards the snowpack bottom, the d-excess profiles of the two snow pits differed somewhat. The snow pit 2 (P2) simply undergone a progressive

decrease to 13.8‰. In contrast, the P1 values first decreased to a minimum of 12.5‰ at 105 cm, and then experienced an increase to 18.3‰ at the base (Figs. 2 and 3).

4.3. Back-trajectory analysis

Following the proposed regional classification (Fig. 4) and considering the different altitudes at which the back-trajectories were evaluated, significant variability was observed in September 2018 at 500 m a.g.l. Local back-trajectories predominated (47%), followed by those from North Central Asia and the Caspian Sea (13% each), while the Mediterranean Sea and Northern India contributed 10% each, and the Arabian Sea accounted for the remaining 7%. At 1500 m a.g.l., local trajectories even more dominant (70%), with the Mediterranean Sea (13%) and Northern India (17%) being the only other notable contributors, and no trajectories from North Central Asia, the Caspian Sea or the Arabian Sea. Although September 2018 is not part of the accumulation season, we included this month to observe the preceding back-trajectory trends. In October 2018, the pattern at 500 m a.g.l. showed an increase in local trajectories (52%) and those from the Caspian Sea (35%), with North Central Asia steady at 13%. At 1500 m a.g.l., compared to 500 m a.g.l., local trajectories increased to 65%, while contributions from the Caspian Sea and North Central Asia decreased to 32% and 3%, respectively. By November 2018, 500 m a.g.l. trajectories were more diverse, with the Middle East (28%) becoming the dominant source, and the Caspian Sea, Mediterranean Sea and Persian Gulf each contributing 20%, alongside a minor influence from Siberia (12%). In contrast, at 1500 m a.g.l., the Mediterranean Sea dominated (67%), followed by the Middle East (33%), with no contributions from the Caspian Sea, Persian Gulf or Siberia. December 2018 at 500 m a.g.l. saw dominance from the Black/Caspian Sea regions, but at 1500 m a.g.l., the Mediterranean Sea was the sole contributor, a trend that continued into January 2019. In January,
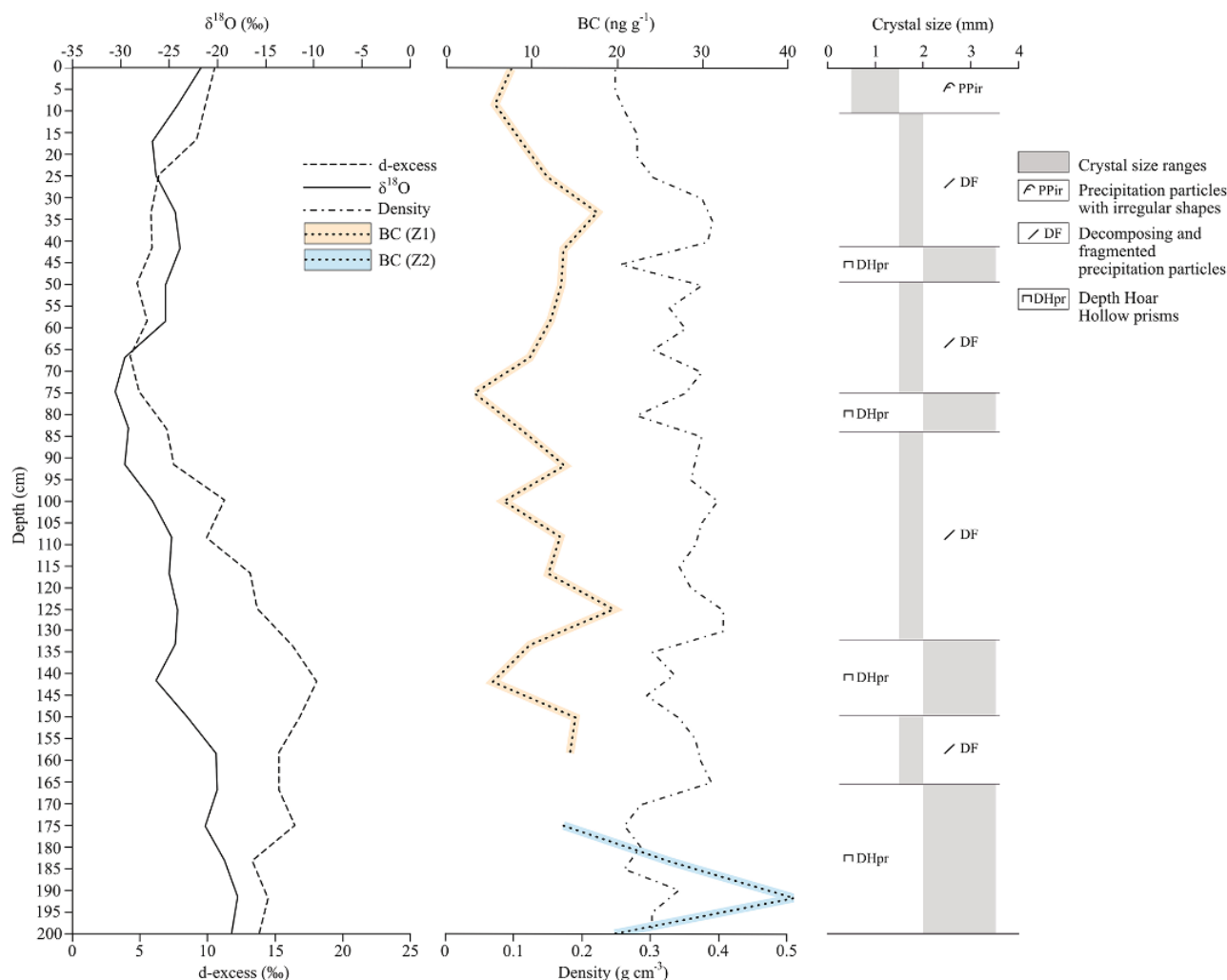
Figure 3. Measurements along P2. (Left) Isotopic variations with $\delta^{18}O$ (top) and d-excess (bottom). (Centre) variation in black carbon (BC) concentrations (top) with differentiation between zones Z1 (orange) and Z2 (blue), along with mass density fluctuations (bottom). (Right) Evolution of grain size range with depth and grain shape classification according to Colbeck (1990) and Fierz and others (2009).

the influence of the Black/Caspian Sea decreased to 55% at 500 m a.g.l., with the Mediterranean Sea (13%) and Persian Gulf (32%) reappearing, though at 1500 m a.g.l., neither the Persian Gulf nor Caspian Sea were present. Finally, in February 2019, at 500 m a.g.l., the Caspian Sea was absent, replaced by the Middle East (46%). Mediterranean Sea comprised by 43%, with smaller contributions from the Persian Gulf (7%) and Siberia (4%). At 1500 m a.g.l., the Mediterranean Sea (40%) and Middle East (25%) origins persisted, with a reappearance of the Caspian Sea (29%) and no contribution from the Persian Gulf, while Siberia remained steady at 4% (see bars in Fig. 6).

4.4. BC concentrations

For BC quantification, the snow pit profiles (P1 and P2) showed data gaps similar to those in the isotopic record; additionally, we collected surface snow samples from K2 high-altitude Camps 1 and 2. In P1, the BC concentration ranged from 5 to 44 ng g^{-1}, with an average value of 14 ng g^{-1}. Meanwhile, in P2, the concentration ranged from 2 to 28 ng g^{-1}, with an average of 10 ng g^{-1}. If we combine the BC concentrations of both snow pits, the average value is 12 ng g^{-1}. Based on concentration levels and fluctuation patterns,

we divided the BC profiles into two main zones: Zone 1 (Z1) and Zone 2 (Z2). In P1, the average BC concentration in Z1 was 8 ng g^{-1}, with this zone extending to a depth of 77 cm. Conversely, in P2, the Z1 average concentration was comparable to P1 (8 ng g^{-1}), but it extended deeper, reaching 160 cm. Zone 2 (Z2) expanded from the limit with Z1 to the snowpack–glacier ice interface and exhibited a higher variability and values. In P1, Z2 average concentration was 27 ng g^{-1}, with maximum values reaching 44 ng g^{-1}, while in P2, the average concentration was 18 ng g^{-1}, with maximum values of 29 ng g^{-1}. Finally, regarding the high-altitude camps, the average concentration for Camp 1 was 7 ng g^{-1}, and 26 ng g^{-1} for Camp 2 (Figs. 2 and 3).

Observations in the snow pits revealed darker layers, especially in P1, where a basal-dark layer aligns with higher BC concentrations (Fig. S1). Another layer at ∼80 cm depth lacked chemical data, leaving its cause – BC or mineral dust – undetermined. Although beyond the scope of this article, mineral dust, common in HMA due to the nearby Taklamakan Desert, also contributes to snow darkening, increasing albedo and accelerating melt (Ge and others, 2014; Jia and others, 2015; Chen and others, 2017; Yuan and others, 2019; Xing and others, 2024).
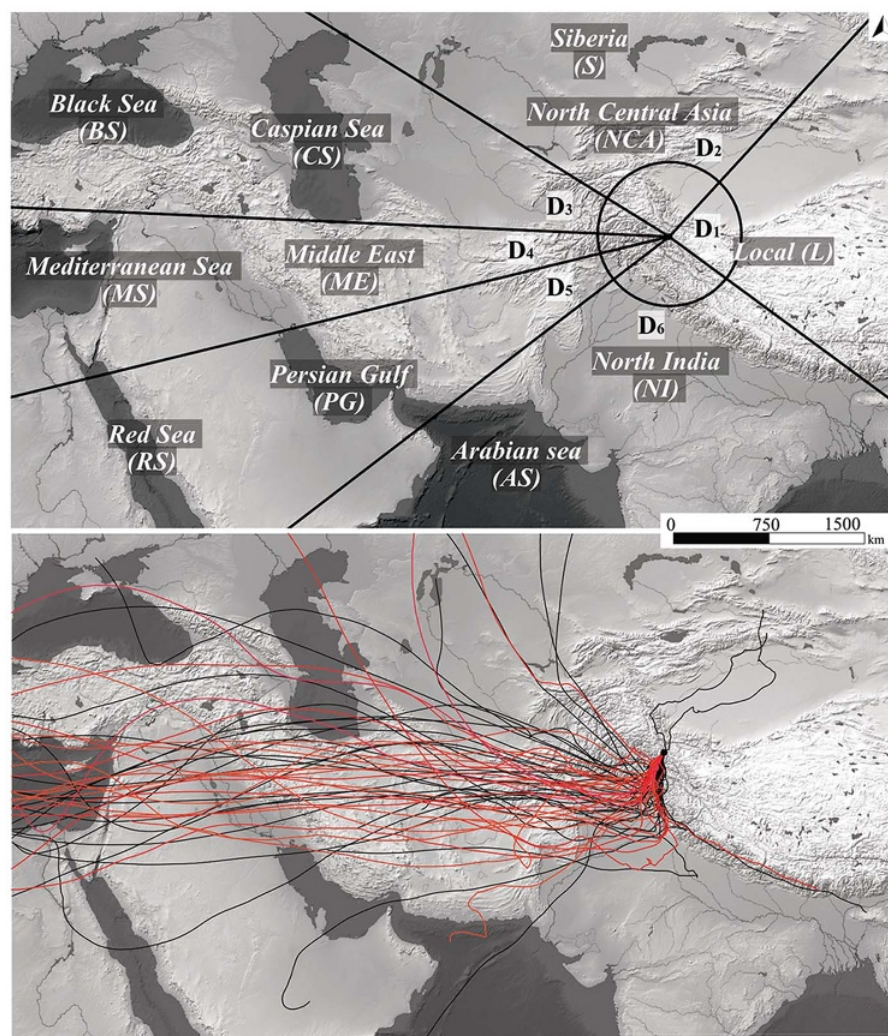
Figure 4. (Top) Geographic divisions used for back-trajectory classification (domains; D1 to D6). (Bottom) Clusters generated from 180 daily back-trajectories (September 2018 to February 2019) at 500 m a.g.l. (black lines) and 1500 m a.g.l. (red lines).

4.5. BC effects on the snowpack

According to the daily data provided by ERA5 (Hersbach, 2016), during the 2019 melting season, the shortwave solar irradiance (I) varied between 242.24 and 0.0035 W m^{-2}, with an average value of 106.68 W m^{-2}. Another necessary parameter obtained from ERA5 was the average CF, which was 0.6. We only considered the data corresponding to daylight hours for I and CF; therefore, values during night-time ($I = 0$ W m^{-2}) do not affect the average. For the calculation of the mean snow crystal radius (r), the grains that made up the intermediate and basal low-density layers, with radii ranging between 2 and 3.5 mm, were excluded, as these crystals result from post-depositional processes, a fact discussed in the following section. Therefore, we considered the average ice crystal radius was 1.5 mm. It is crucial to mention that we made only approximations to obtain a general overview of the potential consequences of the BC concentrations found in the snowpack. The results provide an initial idea, but it is essential to interpret them with caution since they are preliminary estimates rather than a comprehensive and precise assessment.

To perform the quantitative analysis, we took the average shortwave solar irradiance as a reference value (106.68 W m^{-2}). Concerning the snowpack BC concentration, our focus is not on variations along each snow pit, as we did with the isotopic profiles,

but rather on the overall bulk concentration of both combined. The BC load in the Godwin-Austen Glacier snowpack ranged from 2 to 44 ng g^{-1}, with an average of 12 ng g^{-1}. Given the high capacity of BC particles to absorb shortwave solar irradiance, they induce the snowpack to absorb additional energy ranging from 7.8 to 50.35 MJ m^{-2}, with an average of 22.1 MJ m^{-2}. In turn, this increase in energy absorption would reduce the snowpack surface albedo by between 0.0068% and 0.044%, with an average of 0.019%. The extra energy absorption would lead to snowpack warming and, consequently, a positive radiative forcing ranging from +0.73 to +4.73 W m^{-2}, with an average of +2.07 W m^{-2}. These data allow us to estimate the volume of snow that melted sooner per unit area, ranging from 23.3 to 150.7 mm w.e. (or kg m^{-2}), with an average of 66 mm w.e. Regarding the BC load in the high-altitude K2 camps, it could have produced a volume of melted snow of 45.6 mm w.e. in Camp 1 and 109.9 mm w.e. in Camp 2 (Table 1).

5. Discussion

5.1. Snowpack temporal scale

The correct interpretation of BC concentration data requires determining the time interval of the snowpack accumulation, as the

Table 1. Black carbon (*BC*) concentration in the snow pits (P1 and P2) and K2 high-altitude camps (camp 1 and camp 2), and its effects on snow considering the average shortwave irradiance (106.68 w m^{-2})

	BC (ng g^{-1})	ΔA (%)	*RF* (W m^{-2})	*Ex* (MJ m^{-2})	*W* (mm w.e.)
P$_{1,2}$ Minimum	2	−0.0068	+0.73	7.8	23.3
P$_{1,2}$ Maximum	44	−0.044	+4.73	50.35	150.7
P$_{1,2}$ Average	12	−0.019	+2.07	22.1	66.0
Camp 1	7	−0.013	+1.43	15.2	45.6
Camp 2	26	−0.032	+3.45	36.7	109.9

ΔA: albedo reduction, *RF*: radiative forcing, *Ex*: extra energy absorbed by the snowpack, *W*: snow melting sooner.

implications of BC levels in a multi-year snowpack differ from those in a seasonal one. To address this, we focused on water stable isotopes, examining the correlation between δ^{18}O values and temperature, as well as the relationship between moisture sources and d-excess levels. However, it should be considered that the original isotopic composition of the snowpack may be altered from its state at the time of deposition.

The low-density surface layers are likely the result of recent snowfall (Colbeck and others, 1990; Fierz and others, 2009). The crystals with well-defined faces and edges in the middle and basal low-density layers are characteristic of depth hoar (DH; Seligman, 1936). The DH crystals typically form under high-temperature gradients (Akitaya, 1974; Colbeck, 1982; Figs 2 and 3), as observed in the Godwin-Austen snowpack (∼6ºC m^{-1}). The development of DH crystals was more pronounced in P1, possibly due to a greater temperature gradient relative to the snowpack thickness, while higher gradients in the upper 60–80 cm (up to ∼18ºC m^{-1}; Flin and Brzoska, 2008) may explain the middle DH layers (Fig. S3). High-temperature gradients, such as those associated with DH, stimulate molecular diffusion within the pore space, which can potentially alter the isotopic signal in the snowpack. Similarly, diffusion at the snowpack surface may occur due to interactions with the atmosphere (Ekaykin and others, 2002; Konishchev and others, 2003). In this vein, no δ^{18}O variations were detected in relation to the DH layers. However, the higher d-excess values in the DH basal layer of P1 likely suggest intense diffusion, presumably related to the greater development of DH crystals. In the case of surface diffusion, the high precipitation during the 2018–19 winter in the Karakoram region likely preserved the original isotopic signal by reducing atmospheric exchange (IMD, 2019; National Weather Forecasting Centre, 2019). This was further supported by ERA5 data, which identified 2018–19 as one of the three wettest seasons of the past decade, with an average daily precipitation of 2.20 mm w.e. (Fig. S4).

Given the minimal alteration of isotopic values, ERA5 reanalysis (Hersbach, 2016) was employed to estimate temperatures for the entire accumulation season (October 2018–April 2019) and correlate them with δ^{18}O levels in the snowpack. Despite its lower accuracy and resolution compared to the AWS data (available for only 24 days starting on 3 February 2019), ERA5 effectively replicates the temperature patterns recorded by the AWS, making it a reliable tool for assessing long-term trends, even with an underestimation of ∼5ºC. For the correlation, data from P2 (200 cm) was prioritized over P1 (120 cm) due to its location, which provides greater relief, allowing for more vertical accumulation and better protection from erosion. Consequently, the snowpack thickness in P2 was equated to the accumulation season, with the snow–ice interface corresponding to approximately October 2018 and the snowpack surface marking late February 2019, when the snow

pits were excavated. The δ^{18}O variations in P2 closely followed the ERA5 atmospheric temperature patterns (Fig. 5). Temperatures peaked at −14ºC at the start of the season (October 2018), dropped to −32.7ºC in late December 2018, and rose again to −25ºC by late February 2019. Similarly, δ^{18}O peaked at −17.8‰ in October 2018, reached a minimum of −30.5‰ in early January 2019 and increased to −21.7‰ by the end of February 2019.

To confirm the relative scale of the snowpack suggested by the δ^{18}O-temperature correspondence, similar correlations can be established between the d-excess levels along P2 and the origin of the predominant trajectories during the accumulation period (Fig. 6). During October and November 2018, the high average d-excess value (16‰) coincided with a strong influence from westward trajectories (Mediterranean and Middle East). Local moisture recycling processes, such as re-evaporation or evapotranspiration, may have also contributed to these elevated d-excess values (Froehlich and others, 2008; Aemisegger and others, 2014). The values decreased to ∼5‰ in late December 2018 and early January 2019, likely due to the dominance of Black Sea and Caspian Sea trajectories at 500 m a.g.l., typically associated with low d-excess values in winter (Juhlke and others, 2019). By February 2019, d-excess rose again to 10‰, probably due to the return of westward trajectories. These variations can be divided into two groups: higher d-excess values in October–November 2018 and late February 2019 (10.2‰), and lower values from December 2018 to early February 2019 (7.5‰). The corresponding Local Meteoric Water Lines for these groups reveal different intersections with the *y*-axis (d-excess) compared to the GMWL, confirming the distinct origins of the air masses (Fig. S5). Therefore, this correspondence further reinforces the seasonal nature of the snowpack.

Finally, to establish a relationship between P1 and P2, d-excess variations were compared, as their patterns were more distinct, although δ^{18}O variations were also considered. Four comparable sections (S1–S4) were identified between both profiles (Fig. 7). The basal section (S1) showed the highest δ^{18}O values, with similar d-excess patterns, except for a peak in P1, likely due to intense molecular diffusion. In S2, maximum d-excess values were comparable. In S3, δ^{18}O reached a minimum, with corresponding lower d-excess values in both profiles. Finally, the last section (S4) displayed similar isotopic values in both records. Additionally, three hiatuses (H1–H3) were identified in P1 between the sections, possibly correlating with periods of lower precipitation, which may have increased exposure to erosive factors.

Previous studies have found high winter d-excess values in Central Asia due to moisture from the Eastern Mediterranean (Hussain and others, 2015; Liu and others, 2015; Juhlke and others, 2019). However, the Godwin-Austen snowpack showed low d-excess values during the 2018–19 winter, likely influenced by Black and Caspian Sea trajectories. This highlights the complexity of atmospheric dynamics in the western HMA, particularly during the positive precipitation anomaly of that particular season (Fig. S6; Dimri and others, 2015; Hunt and others, 2018; Attada and others 2022; Nischal and others, 2022).

5.2. Implications of BC-enhanced snowmelt

The clear difference in the BC concentration between Zones 1 (Z1) and 2 (Z2) in both snow pits is consistent with previous studies that reported higher concentrations in the bottom of the snowpack (e.g., Thakur and others, 2021). This distribution can be explained by the partial melting of snow layers formed during snowfalls at the beginning of the accumulation season (autumn), which can
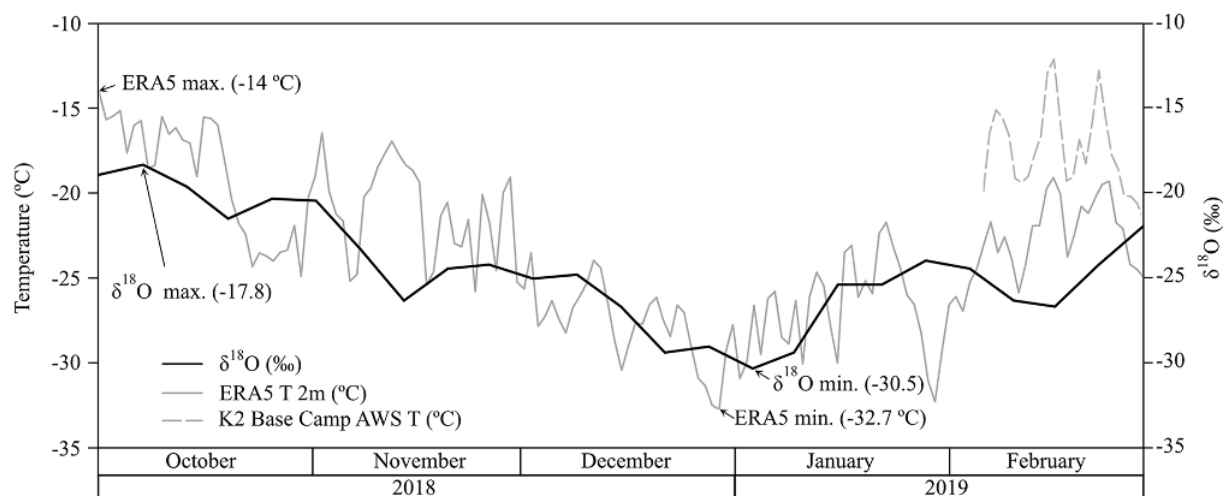
Figure 5. Comparison of $\delta^{18}O$ variation along P2 (black line) with the daily mean temperature values at 2 m above the ground obtained from ERA5 (solid grey line). the temperature values acquired in situ by the Base Camp automatic weather station (AWS) are depicted by the dashed grey line.
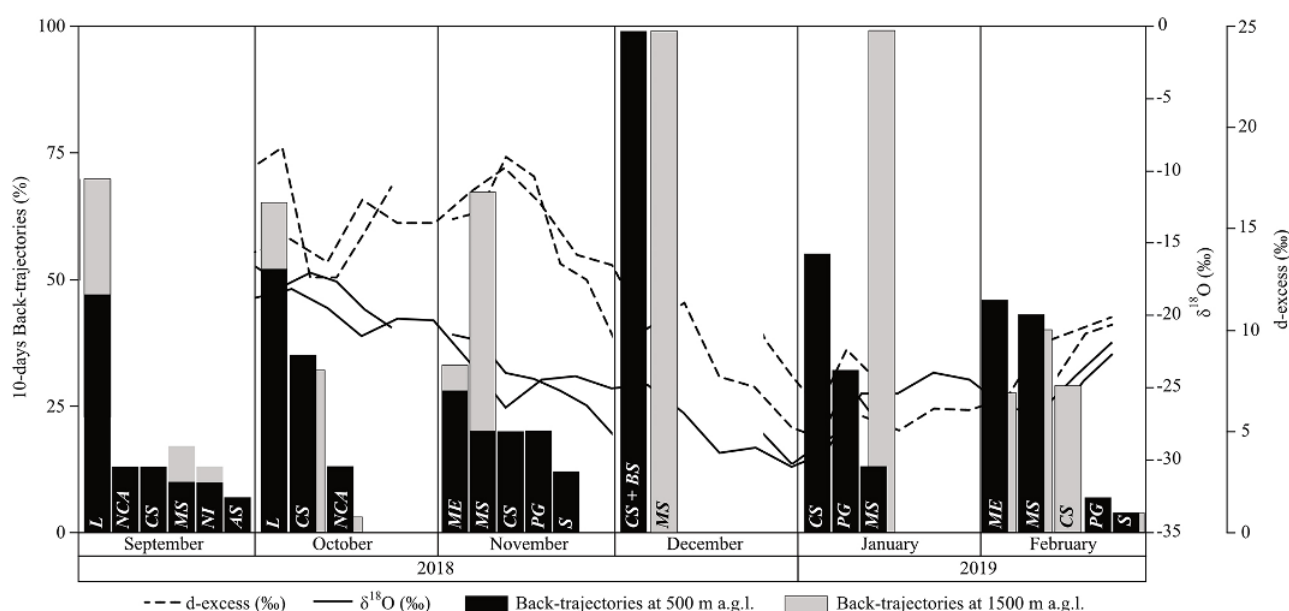

Figure 6. Frequency diagram illustrating back-trajectories contributions to each domain at both altitudeS: 500 and 1500 m a.g.l. isotopic variations of both snow pits (P1 and P2) are depicted behind the bar chart. domain 1 (L: local), domain 2 (NCA: North Central Asia and S: siberia), domain 3 (CS: Caspian Sea and BS: Black Sea), domain 4 (ME: Middle East and MS: Mediterranean Sea), domain 5 (PG: Persian Gulf and RS: Red Sea) and domain 6 (NI: Northern India and AS: Arabian Sea).

potentially concentrate BC particles. This occurs due to the still high solar radiation and the fact that the Godwin-Austen Glacier is debris-covered, that reduces the albedo of its surface, leading to greater absorption of solar energy, increased surface heating and ultimately accelerating the melting of the initial snow layers. As a result, the BC average concentration in Z2 (27 ng g^{-1} in P1 and 18 ng g^{-1} in P2) could be attributed to these reconcentration processes. Conversely, the Z1 average concentration in both snow pits (8 ng g^{-1}), with lower variability compared to Z2, is likely less influenced by reconcentration processes, providing a more accurate depiction of the local average snowpack BC concentration during the 2018–19 winter season and its related effects. Consequently, the BC concentration in Z1 would produce 53 mm w.e. of meltwater.

To give a sense of the scale of meltwater generated by the total average BC during the 2019 melting season (66 mm w.e.), we can reference the average precipitation during the study season (from October to February) over the previous 10 years (2009–19), which was 283 mm w.e. In this context, the meltwater generated could potentially represent ~23%, while considering only Z1, this percentage would reduce to ~18%. However, caution is necessary when interpreting these values due to inherent uncertainties in the data, particularly regarding the accuracy of precipitation estimates, which rely on interpolations from the ERA5 atmospheric reanalysis. Additionally, in remote mountainous regions with limited instrumental data, such as the Karakoram, ERA5 often struggles to capture local precipitation dynamics accurately. Furthermore, the average BC concentration is based on measurements from only
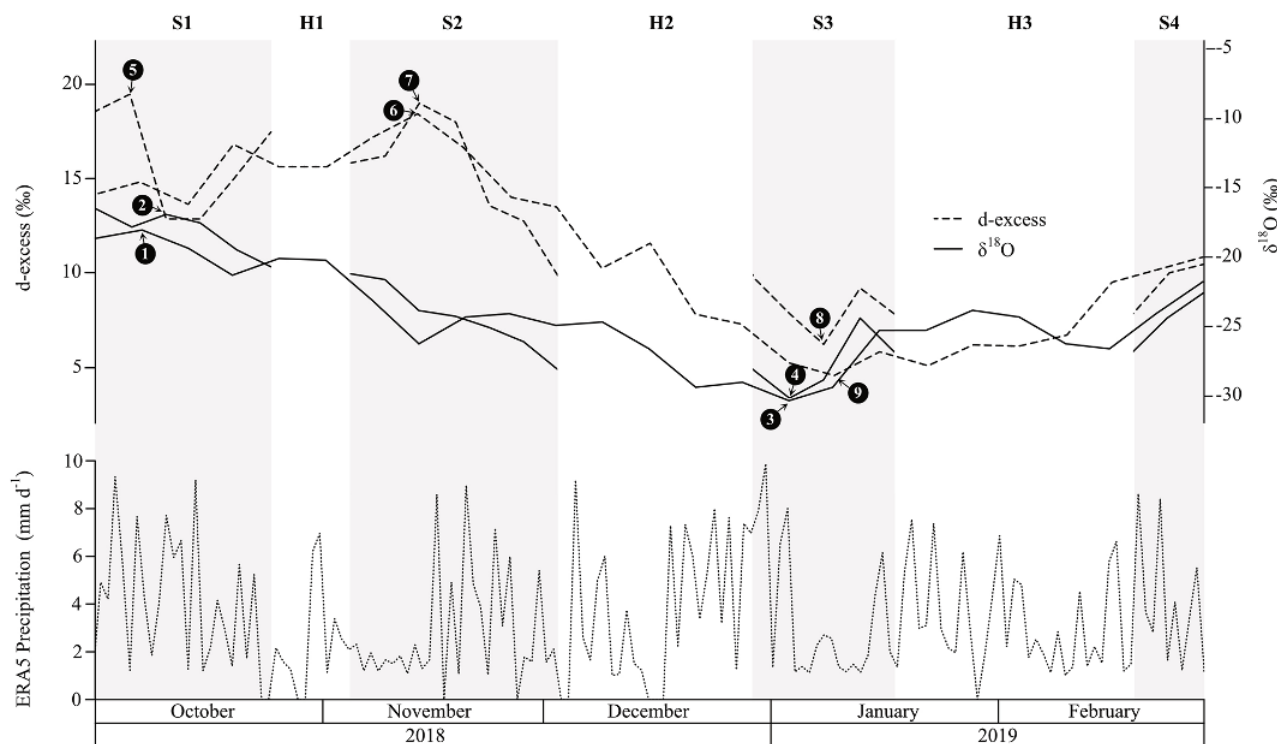
Figure 7. (Top) potential correlations between P1 and P2 based on their Isotopic variations: $\delta^{18}O$ (solid lines) and d-excess (dashed lines). (1) P2 $\delta^{18}O$ max. (−17.8‰), (2) P1 $\delta^{18}O$ max. (−16.3‰), (3) P2 $\delta^{18}O$ min. (−30.5‰), (4) P1 $\delta^{18}O$ min. (−30.4‰), (5) P1 d-excess max. (19‰), (6) P2 d-excess max. (18‰), (7) P1 d-excess 2nd max. (18.6‰), (8) P1 d-excess min. (6.1‰), (9) P2 d-excess min. (4.4‰). correlation sections are depicted as grey bands with the letter S, while sections with missing records in P1 appear as white bands with the letter h (hiatus). (Bottom) seasonal precipitation data (dotted line) from ERA5. Hiatuses (H) may correspond to periods characterised by less frequent and/or less intense total precipitation events.

two isolated points on the glacier (P1 and P2), which limits the representativeness of the data. Regarding the BC load in surface snow at high-altitude camps, we cannot quantify the effects in the same way as we did for the snowpack, since these are even more localized measurements, as they are limited to surface snow samples. However, their analysis provides insights into how the presence of this pollutant impacts regions at high altitudes and how the activities conducted at these camps contribute to environmental contamination. In this context, the presence of this pollutant could produce 45.6 mm w.e. of meltwater at Camp 1, increasing to 109.9 mm w.e. at Camp 2.

5.3. Potential local and regional BC sources

The Baltoro and Godwin-Austen Glaciers serve as the main route to the base camps of K2 and Broad Peak, involving a seven-day trek over ice and debris (see Fig. 1b). Expeditions set up temporary camps near permanent army bases, both reliant on kerosene for cooking and heating. During our expedition, the AWS at K2BC recorded predominant strong winds (>10 m s^{-1}) from the west (Saboy Glacier), with some from the northwest and fewer from the south, suggesting limited pollutant dispersion from K2BC to the snow pit sites. The minimal impact from nearby camps like Concordia, located southward, can be attributed to the infrequency of southern winds (Fig. S7). This indicates that the BC average concentration in the snow pits (12 ng g^{-1}) may be representative of the overall concentration in the Godwin-Austen snowpack for the 2018–19 season, with contributions from distant and local sources.

Although no wind data are available prior to 3 February 2019, similar patterns were observed starting from early January 2019.

To evaluate regional BC sources, we used monthly average atmospheric concentrations from the MERRA-2 atmospheric reanalysis (Fig. S8). Between September 2018 and December 2019, BC concentrations increased across South Asia, followed by a decrease from January to February 2019. This trend was particularly notable in the Indo-Gangetic Plain (IGP), where concentrations reached up to 8 µg m^{-3} in December 2018. This increase was influenced by high population density, industrialization, higher heating demand due to lower temperatures and a lack of precipitation, which reduced BC removal through wet deposition. Additionally, the surrounding mountain ranges, such as the Himalayas to the north and the Safēd Kōh Range to the west, acted as barriers, limiting the dispersion of pollutants. Furthermore, from September 2018 to February 2019, other regions of Central Asia and the Middle East exhibited similar patterns of BC atmospheric concentration, though to a lesser extent.

By combining BC atmospheric concentration with back-trajectories, we can estimate the contribution of long-distance BC sources to the snowpack during the accumulation period (Fig. S8). In September and October 2018, the main sources at 500 and 1500 m a.g.l. were the northern Indus River basin lowlands, with secondary contributions of South Asia, eastern IGP, the Middle East, Central Asia and Western China. In November 2018, the Middle East was the major contributor at 500 m a.g.l., followed by Central Asia and the Near East. In December 2018, the westerly jet stream increased the contribution of Central Asia, Eastern Europe, the Middle East and the Near East, while the northern

Table 2. Summary of BC studies in snow across the HMA region

Subregion	Code	Study area	Alt. (m a.s.l.)	Season	Type	n	Depth (cm)	BC (ng g⁻¹) Min.	Max.	Avg.	Ref.
Tibetan Plateau	5	Qiangyong (Gl.)	5400	–	Ss	1	n/a	–	–	43	Xu and others, 2006
	12	Zhadang (Gl.)	5720–5795	Sum.	SsA	2	n/a	34	67	50	Qu and others, 2014
	11	Zhadang (Gl.)	5507–5795	Sum.	SsF	8	n/a	41	59	52	Qu and others, 2014
	9	Zhadang (Gl.)	5570–5790	Spr./Sum.	Ss	13	n/a	54	627	59	Li and others, 2018
	17	La'nong (Gl.)	5850	Sum.	Swp	3	28	22	97	67	Ming and others, 2009
	4	Dongkemadi (Gl.)	5600	–	Swp	4	52	18	168	79	Xu and others, 2006
	18	Zhadang (Gl.)	5800	Sum.	Swp	8	40	32	600	114	Ming, 2009
	10	Zhadang (Gl.)	5790	Spr.	Swp	14	138	118	1224	303	Li and others, 2018
	3	Meikuang (Gl.)	5200	Sum.	Ss	1	n/a	–	–	446	Xu and others, 2006
Himalayas	7	Namunani (Gl.)	5780–6080	–	Ss	7	n/a	0	10	4	Xu and others, 2006
	27	Khumbu (Reg.)	5079–5700	–	Ss	56	n/a	0	70	10	Jacobi and others, 2015
	19	East Rongbuk (Gl.)	6465	Aut.	Swp	1	100	–	–	18	Ming and others, 2009
	6	Kangwure (Gl.)	6000	–	Ss	1	n/a	–	–	22	Xu and others, 2006
	28	Mera (Gl.)	5800	Spr./Aut.	Swp	–	200	–	318	24	Kaspari and others, 2014
	25	Durga Kot (Gl.)	4950	Sum.	Swp	4	30	13	327	160	Svensson and others, 2018
	26	Bhanolti (Gl.)	5008	Sum.	Swp	15	120	57	608	169	Svensson and others, 2018
	39	Western Himalayas (Reg.)	3500–5000	Sum.	Ss	42	n/a	13	76	–	Thind and others, 2019
Tienshan	24	Urimiqi No.1 (Gl.)	4050	Sum.	Ss	5	n/a	23	30	27	Ming and others, 2016
	14	Haxilegen River No.48 (Gl.)	3755	Aut.	Swp	9	90	11	981	87	Ming and others, 2009
	13	Miao'ergou No.3 (Gl.)	4510	Sum.	Swp	3	70	81	139	107	Ming and others, 2009
	21	Urimiqi No.1 (Gl.)	>4130	Sum.	Ss	–	n/a	250	500	–	Xu and others, 2012
	22	Urimiqi No.1 (Gl.)	>4130	Spr./Aut.	Ss	–	n/a	60	150	–	Xu and others, 2012
	23	Urimiqi No.1 (Gl.)	>4130	Win.	Ss	–	n/a	27	31	–	Xu and others, 2012
Karakoram	41	K2 Camp1	6076	Win.	SsF	2	n/a	–	–	7	This study
	40	Godwin-Austen (Gl.)	4927–4937	Win.	Swp	43	200	2	44	12	This study
	42	K2 Camp2	6650	Win.	SsF	1	n/a	–	–	26	This study
	37	Kalam (Loc.)	1933–2101	Win.	SsF	4	n/a	79	123	107	Gul and others, 2018
	32	Kardug (Gl.)	5340	Sum.	Swp	20	100	40	312	114	Thakur and others, 2021
	33	Phuche (Gl.)	5613	Sum.	Swp	30	150	59	299	127	Thakur and others, 2021
	38	Sost (Loc.)	2873–3092	Win.	SsA	6	n/a	482	5957	2506	Gul and others, 2018
Altai	34	Koktokay (S.St.)	1375	Win.	Ss	47	n/a	–	–	2	Zhang and others, 2023
	36	Koktokay (S.St.)	1375	Win.–Spr.	Ss	47	n/a	0	13	6	Zhang and others, 2023
	35	Koktokay (S.St.)	1375	Spr.	Ss	47	n/a	–	–	6	Zhang and others, 2023
Qilian	16	Qiyi (Gl.)	4850	Sum.	Swp	2	34	21	24	22	Ming and others, 2009
	15	Laohugou No.12 (Gl.)	5045	Aut.	Swp	2	30	32	39	35	Ming and others, 2009
	20	Laohugou No.12 (Gl.)	4350–4600	Win.	Ss	12	n/a	611	11040	2942	Zhang and others, 2017
	1	July 1st (Gl.)	4600	Sum.	P	4	n/a	2	9	7	Xu and others, 2006
	2	July 1st (Gl.)	4600	Sum.	SsA	5	n/a	30	76	53	Xu and others, 2006
Pamirs	30	Muji (Gl.)	4910–5460	M.S.	SsF	–	n/a	–	–	25	Yang and others, 2015
	8	Muztagh Ata (Gl.)	6350	–	Swp	6	180	16	182	52	Xu and others, 2006
	31	Muji (Gl.)	4910–5460	M.S.	SsA	–	n/a	–	–	326	Yang and others, 2015

Studies are organized by subregion and listed in ascending order of average BC concentration. Geographic locations are indicated by corresponding codes in Fig. 8. The 'Study area' indicates the type of location: glacier (Gl.), region (Reg.), locality (Loc.) or snow station (S.St.). Seasons are abbreviated as Sum. (summer), Spr. (spring), Aut. (autumn), Win. (winter) and M.S. (melting season). Sample types include Ss (surface snow), SsA (aged surface snow, > 24 h post-deposition), SsF (fresh surface snow, <24 h post-deposition), Swp (snow pit) and P (precipitation). The letter 'n' indicates the number of samples, and 'depth' refers to the maximum snow pit depth (n/a for surface snow samples). The BC concentrations are given in ng g⁻¹, with minimum, maximum and average values provided. A dash (-) indicates unavailable or unspecified data. The 'Ref.' column contains the reference of each study.
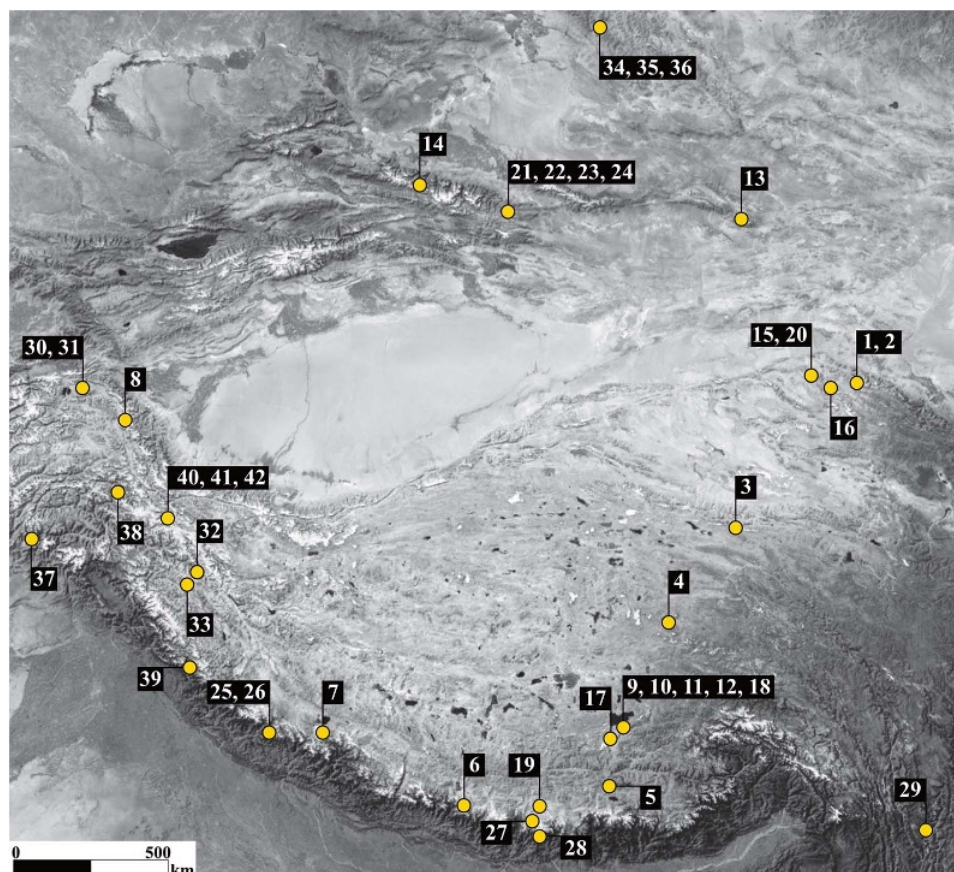
Figure 8. Locations and distribution of studies focused on BC in snow across HMA. Each code (number) corresponds to a study listed in Table 2.

Indus basin lost influence. The trajectories at 1500 m a.g.l. from November 2018 to February 2019 show a similar contribution to that of December 2018 at 500 m a.g.l. Continuing at 500 m a.g.l., in January 2019, the westerlies persisted, but some clusters may have carried BC from the central Gangetic Plain. In February 2019, contributions mainly came from the West, with influence from the Persian Gulf region, Middle East, and, to a lesser extent, from Central Asia. The connection between BC distant sources and back-trajectories is an estimation with inherent limitations: BC concentration in the snowpack does not reflect accurately the predominant long-distance sources due to factors like dry or wet deposition (outputs) and inputs from regions along the transport path.

The trajectories during the accumulation season in K2 Camps 1 and 2 matched those for the snow pits, likely due to the nearby sampling points and the resolution of meteorological data used in HYSPLIT. Even with a higher resolution, the general patterns would not have important variations, so we consider this result valid. High-altitude snow samples were taken at the end of February 2019, coinciding with snow pit sampling. The BC values at K2 Camp 1 (6076 m a.s.l.; 7 ng g^{-1}) were similar to surface snow in the snow pits, constituting a reliable representation of BC concentration in the surface snow during late February 2019. In contrast, Camp 2 (6650 m a.s.l.) had much higher concentrations (26 ng g^{-1}), likely due to activities from successive expeditions, indicating their impact on the high-mountain environment.

5.4. Godwin-Austen Glacier BC in HMA: A comparison

The HMA region consists of several sub-regions, each influenced by distinct BC sources and atmospheric patterns (Table 2; Fig. 8). In comparing results across studies, it is important to consider that differences in sampling methodologies and post-depositional processes can alter BC concentrations and their effects. Snow pit excavation studies generally follow one of two approaches: either calculating the average BC concentration for the entire snowpack and treating it as a representative value, or conducting a more detailed layer-by-layer analysis, which requires higher sampling resolution. Additionally, surface snow sample analyses show that BC concentrations can fluctuate based on the time between deposition and sampling. Some studies also distinguish between precipitation snow and freshly fallen snow, as BC concentrations can change even over short periods. Surface snow modification mainly results from phase changes, which are primarily influenced by temperature variations linked to altitude and seasonality. As a result, in lower-elevation areas and warmer seasons, surface snow undergoes more significant modification, while at higher altitudes and during colder seasons, these changes are less pronounced. Selecting the sampling point appropriately is crucial, taking into account local BC sources, their proximity, and potential influences (e.g., industrial areas, urban areas or roads), as these factors can lead to an overestimation of background BC levels.

Due to the heterogeneity of sampling conditions, in terms of seasonality, altitude and methods, establishing a direct comparison

between our data and previous studies would be inappropriate, even if some values are similar. To address this issue, it is crucial to define clear standard criteria, such as the maximum depth to consider a sample as surface snow. The lack of well-defined criteria in the literature can lead to ambiguous interpretations and hinder data comparability. Besides, following and reporting sampling protocols is essential to maintain data integrity, including using sterilized materials and personal protective equipment, especially in isolated areas with low concentrations, such as our study site. Nevertheless, conducting a comparative analysis of existing BC studies in the HMA region would be a valuable exercise to situate our study within a broader context (Table 2).

Compared to previous snow pit excavation studies, the work conducted on the Godwin-Austen Glacier is notable as the only study performed during the winter season, since this type of fieldwork is often carried out in the summer. Two factors may explain why the average BC concentration in our snow pits (12 ng g^{-1}) is significantly lower than the average concentration reported in previous snow pit-based studies (127 ng g^{-1}). First, the concentration in summer studies is likely influenced by BC reconcentration processes resulting from snowmelt. Second, the unusually high snow accumulation during the winter of 2018–19 may have diluted BC levels. These factors also account for the fact that the snow pits in this study recorded both the lowest minimum BC concentration (2 ng g^{-1}) and one of the lowest maximum concentrations (44 ng g^{-1}) in the dataset. Our snow pits reached a depth of 200 cm, only comparable to the study of Kaspari and others (2014) on the Mera Glacier (Himalayas), and included the highest number of samples (43). In terms of altitude, the snow pits were excavated at a relatively lower average elevation ($\sim$4930 m a.s.l.) compared to the average elevation of $\sim$5330 m a.s.l. observed in similar studies. This difference is likely due to the more favourable summer conditions for snow pit excavation. Notably, this investigation is one of the few conducted in the Karakoram region, alongside the studies by Thakur and others (2021) on the Kardung and Phuche glaciers.

Surface snow studies are common throughout the HMA, as they are more time-efficient and less labour-intensive compared to snow pit excavations. These samples are typically collected at an average altitude of $\sim$4740 m a.s.l., with the samples from Camp 1 (6076 m a.s.l.) and Camp 2 (6650 m a.s.l.) standing out due to their significantly high altitudes. They also exhibit greater seasonal heterogeneity, with samples collected during spring, autumn and winter. The average BC concentration in the dataset of 193 ng g^{-1} is significantly higher than the concentrations found in our samples, which range from 7 to 26 ng g^{-1}. The BC concentrations in the winter surface snow samples are expected to be low due to higher accumulation rates and reduced melting, but the exceptionally high concentrations reported by Zhang and others (2017) and Gul and others (2018) skew the winter average concentrations of the dataset to 1112 ng g^{-1}. Excluding these outliers, the average drops significantly to 38 ng g^{-1}. However, it is important to note that our study has one of the lowest levels of sample representativity for surface snow compared to previous studies in the region.

6. Conclusions

This work presents the first attempt to quantify the BC concentration in the seasonal snowpack over the Godwin-Austen Glacier, Central Karakoram Range, Pakistan. To achieve this, we used snow samples extracted from two snow pits (P1 and P2) excavated south of the K2BC, along with surface snow samples from K2 Camps 1 and 2.

The alignment between the δ^{18}O profile and temperature records from ERA5 reanalysis and the K2BC AWS, along with the correlation of d-excess variations with potential source trajectories during the accumulation season, suggests that the studied snowpack has a seasonal character, having accumulated at the beginning of the accumulation season around October 2018 and disappeared during the 2019 ablation season. Determining the timing of snowpack formation is essential for accurately interpreting BC data.

The back-trajectory analysis reveals shifts in dominant regional BC sources during the accumulation season, with contributions from the northern Indus basin in early autumn, followed by increasing influence from the Middle East, Central Asia and Eastern Europe through winter. Local sources, including army camps and base camps, such as the K2BC, also contribute significantly to BC levels in the area. Together, these sources account for the BC concentrations observed in the Godwin-Austen Glacier snowpack. Based on snow pit samples, the average BC concentration is 12 ng g^{-1}. The similar surface concentrations and close sampling dates of the snow pit and surface snow samples at K2 Camp 1 ($\sim$7 ng g^{-1}) suggest that this concentration may represent the prevailing BC level in the area in late February 2019. The elevated BC average concentration in the lower section (Z2) of the snowpack (ranging from 18 to 27 ng g^{-1}) could result from early-season snowmelt and subsequent particle reconcentration, indicating that the average concentration measured in Z1 (8 ng g^{-1}) may be more representative. Additionally, the high concentration observed at Camp 2 (26 ng g^{-1}) likely reflects the impact of mountaineering activities and their associated environmental effects.

Considering the average solar irradiance (106.68 W m^{-2}) and mean BC concentration, BC-induced albedo reduction caused 66 mm w.e. of snow to melt sooner during the 2019 melting season. To contextualize these findings, this would represent $\sim$23% of the regional average precipitation volume measured over the past 10 years for the same reference period, from October to February. This percentage decreases to 18% when considering the lower concentration in Z1. However, caution is necessary due to data limitations and reliance on a small number of sampling points.

When comparing the results with previous studies, it is important to consider that variability in BC concentrations in the snow across the HMA region is influenced by diverse sources and atmospheric patterns. Besides, differences in sampling methodologies and post-depositional processes complicate direct comparisons of results. Consequently, to ensure reliable data comparability, standardized sampling criteria and protocols, along with consideration of local BC sources, are essential.

mountaineers for their logistic support and willingness to collect snow samples from the K2 camps. Finally, we extend our gratitude to Deniz Bozkurt from the University of Valparaiso for his valuable contributions.

Competing interests. The authors declare no competing interests for this paper.

References

Aemisegger F, Pfahl S, Sodemann H, Lehner I, Seneviratne SI and Wernli H (2014) Deuterium excess as a proxy for continental moisture recycling and plant transpiration. *Atmospheric Chemistry and Physics* **14**(8), 4029–4054. doi: 10.5194/acp-14-4029-2014

Ahmad S and 8 others (2020) Spatio-temporal trends in snow extent and their linkage to hydro-climatological and topographical factors in the Chitral River Basin (Hindukush, Pakistan). *Geocarto International* **35**(7), 711–734. doi: 10.1080/10106049.2018.1524517

Akitaya E (1974) Studies on depth hoar. *Contributions from the Institute of Low Temperature Science* **26**, 1–67.

Archer DR and Fowler HJ (2004) Spatial and temporal variations in precipitation in the Upper Indus Basin, global teleconnections and hydrological implications. *Hydrology and Earth System Sciences* **8**(1), 47–61. doi: 10.5194/hess-8-47-2004

Attada R and 6 others (2022) Diagnostic evaluation of extreme winter rainfall events over the Arabian Peninsula using high-resolution weather research and forecasting simulations. *Meteorological Applications* **29**(5). doi: 10.1002/met.2095

Baudouin JP, Herzog M and Petrie CA (2020) Cross-validating precipitation datasets in the Indus River basin. *Hydrology and Earth System Sciences* **24**(1), 427–450. doi: 10.5194/hess-24-427-2020

Baumann F, He JS, Schmidt K, Kühn P and Scholten T (2009) Pedogenesis, permafrost, and soil moisture as controlling factors for soil nitrogen and carbon contents across the Tibetan Plateau: Carbon and nitrogen contents across the Tibetan Plateau. *Global Change Biology* **15**(12), 3001–3017. doi: 10.1111/j.1365-2486.2009.01953.x

Bhatti AM, Suttion P and Seigo N (2009) Agriculture water demand management in Pakistan: A review and perspective. Society for Social Management Systems (SSMS)

Bolch T and 11 others (2012) The state and fate of Himalayan glaciers. *Science* **336**(6079), 310–314. doi: 10.1126/science.1215828

Bond TC and30 others (2013) Bounding the role of black carbon in the climate system: A scientific assessment. *Journal of Geophysical Research: Atmospheres* **118**(11), 5380–5552. doi: 10.1002/jgrd.50171

Bookhagen B and Burbank DW (2010) Toward a complete Himalayan hydrological budget: Spatiotemporal distribution of snowmelt and rainfall and their impact on river discharge. *Journal of Geophysical Research* **115**(F3), F03019. doi: 10.1029/2009JF001426

Center For International Earth Science Information Network-CIESIN-Columbia University & Centro Internacional De Agricultura Tropical-CIAT (2005) *Gridded Population of the World, Version 3 (GPWv3): Population Density Grid* [Dataset]. Palisades, NY: NASA Socioeconomic Data and Applications Center (SEDAC).

Chen S and 7 others (2017) Comparison of dust emissions, transport, and deposition between the Taklimakan Desert and Gobi Desert from 2007 to 2011. *Science China Earth Sciences* **60**(7), 1338–1355. doi: 10.1007/s11430-016-9051-0

Chylek P, Videen G, Ngo D, Pinnick RG and Klett JD (1995) Effect of black carbon on the optical properties and climate forcing of sulfate aerosols. *Journal of Geophysical Research* **100**(D8), 16325. doi: 10.1029/95JD01465

Cohen JL (1994) Snow cover and climate. *Weather* **49**, 150–156.

Colbeck SC (1982) An overview of seasonal snow metamorphism. *Reviews of Geophysics* **20**(1), 45. doi: 10.1029/RG020i001p00045

Colbeck SC and 7 others (1990) *The International Classification for Seasonal Snow on the Ground. International Commission on Snow and Ice (IAHS).* Boulder, CO, USA: World Data Center A for Glaciology, University of Colorado.

Cordero RR and 18 others (2022a) Black carbon in the Southern Andean snowpack. *Environmental Research Letters* **17**(4), 044042. doi: 10.1088/1748-9326/ac5df0

Cordero RR and 20 others (2022b) Black carbon footprint of human presence in Antarctica. *Nature Communications* **13**(1), 984. doi: 10.1038/s41467-022-28560-w

Craig H (1961) Isotopic variations in meteoric waters. *Science* **133**(3465), 1702–1703. doi: 10.1126/science.133.3465.1702

Cui L, Song X and Zhong G (2021) Comparative analysis of three methods for HYSPLIT atmospheric trajectories clustering. *Atmosphere* **12**(6), 698. doi: 10.3390/atmos12060698

Dahri ZH and 11 others (2021) Spatio-temporal evaluation of gridded precipitation products for the high-altitude Indus basin. *International Journal of Climatology* **41**(8), 4283–4306. doi: 10.1002/joc.7073

Dang C, Brandt RE and Warren SG (2015) Parameterizations for narrowband and broadband albedo of pure snow and snow containing mineral dust and black carbon. *Journal of Geophysical Research: Atmospheres* **120**(11), 5446–5468. doi: 10.1002/2014JD022646

Dang C, Warren SG, Fu Q, Doherty SJ, Sturm M and Su J (2017) Measurements of light-absorbing particles in snow across the Arctic, North America, and China: Effects on surface albedo. *Journal of Geophysical Research: Atmospheres* **122**(19). doi: 10.1002/2017JD027070

Dansgaard W (1964) Stable isotopes in precipitation. *Tellus* **16**(4), 436–468. doi: 10.1111/j.2153-3490.1964.tb00181.x

Decheng M (1978) *The Map of Snow Mountains in China, K2 (Mount Quogori).* Lanzhou: Chinese Academy of Sciences. Lanzhou Institute of Glaciology and Geocryology.

Dimri AP and 6 others (2015) Western disturbances: A review. *Reviews of Geophysics* **53**(2), 225–246. doi: 10.1002/2014RG000460

Ekaykin AA, Lipenkov V, Barkov NI, Petit JR and Masson-Delmotte V (2002) Spatial and temporal variability in isotope composition of recent snow in the vicinity of Vostok station, Antarctica: Implications for ice-core record interpretation. *Annals of Glaciology* **35**, 181–186. doi: 10.3189/172756402781816726

Epstein S and Mayeda T (1953) Variation of O^{18} content of waters from natural sources. *Geochimica et Cosmochimica Acta* **4**(5), 213–224. doi: 10.1016/0016-7037(53)90051-9

Fierz C and 8 others (2009) The international classification for seasonal snow on the ground. IHP - VII Technical Documents in Hydrology N°83, IACS Contribution N°1, UNESCO-IHP, Paris.

Flanner MG, Zender CS, Randerson JT and Rasch PJ (2007) Present-day climate forcing and response from black carbon in snow. *Journal of Geophysical Research* **112**(D11), D11202. doi: 10.1029/2006JD008003

Flin F and Brzoska JB (2008) The temperature-gradient metamorphism of snow: Vapour diffusion model and application to tomographic images. *Annals of Glaciology* **49**, 17–21. doi: 10.3189/172756408787814834

Friedman I (1953) Deuterium content of natural waters and other substances. *Geochimica Et Cosmochimica Acta* **4**(1–2), 89–103. doi: 10.1016/0016-7037(53)90066-0

Friedman I, Smith GI, Gleason JD, Warden A and Harris JM (1992) Stable isotope composition of waters in southeastern California 1. Modern precipitation. *Journal of Geophysical Research: Atmospheres* **97**(D5), 5795–5812. doi: 10.1029/92JD00184

Froehlich K, Kralik M, Papesch W, Rank D, Scheifinger H and Stichler W (2008) Deuterium excess in precipitation of Alpine regions – Moisture recycling. *Isotopes in Environmental and Health Studies* **44**(1), 61–70. doi: 10.1080/10256010801887208

Galewsky J, Steen-Larsen HC, Field RD, Worden J, Risi C and Schneider M (2016) Stable isotopes in atmospheric water vapour and applications to the hydrologic cycle: Isotopes in the atmospheric water cycle. *Reviews of Geophysics* **54**(4), 809–865. doi: 10.1002/2015RG000512

Ge JM, Huang JP, Xu CP, Qi YL and Liu HY (2014) Characteristics of Taklimakan dust emission and distribution: A satellite and reanalysis field perspective: Taklimakan dust Characteristics. *Journal of Geophysical Research: Atmospheres* **119**(20), 11772–11783. doi: 10.1002/2014JD022280

Gul C and 7 others (2018) Concentrations and source regions of light-absorbing particles in snow/ice in northern Pakistan and their impact

on snow albedo. *Atmospheric Chemistry and Physics* **18**(7), 4981–5000. doi: 10.5194/acp-18-4981-2018

Hartigan JA and Wong MA (1979) Algorithm AS 136: A K-means clustering algorithm. *Applied Statistics* **28**(1), 100. doi: 10.2307/2346830

Hasson SU (2016) Future water availability from Hindukush-Karakoram-Himalaya upper Indus basin under conflicting climate change scenarios. *Climate* **4**(3), 40. doi: 10.3390/cli4030040

Hersbach H (2016) The ERA5 Atmospheric Reanalysis, NG33D–01.

Hewitt K, Wake CP, Young GJ and David C (1989) Hydrological investigations at Biafo Glacier, Karakoram Range, Himalaya; an important source of water for the Indus river. *Annals of Glaciology* **13**, 103–108. doi: 10.3189/S0260305500007710

Hunt KMR, Curio J, Turner AG and Schiemann R (2018) Subtropical westerly jet influence on occurrence of western disturbances and Tibetan plateau vortices. *Geophysical Research Letters* **45**(16), 8629–8636. doi: 10.1029/2018GL077734

Hussain S and 6 others (2015) Controlling factors of the stable isotope composition in the precipitation of Islamabad, Pakistan. *Advances in Meteorology*, 1–11. doi: 10.1155/2015/817513

IMD, India Meteorological department. Monthly Weather Report 2018/2019.

Immerzeel WW and 31 others (2020) Importance and vulnerability of the world's water towers. *Nature* **577**(7790), 364–369. doi: 10.1038/s41586-019-1822-y

Immerzeel WW, Van Beek LPH and Bierkens MFP (2010) Climate change will affect the Asian water towers. *Science* **328**(5984), 1382–1385. doi: 10.1126/science.1183188

IPCC (2013) *The Physical Science Basis. Contribution of Working Group I to the Fifth Assessment Report of the Intergovernmental Panel on Climate Change* [Stocker, T.F., D. Qin, G.-K. Plattner, M. Tignor, S.K. Allen, J. Boschung, A. Nauels, Y. Xia, V. Bex and P.M. Midgley (eds.)]. Cambridge University Press, Cambridge, United Kingdom and New York, NY, USA, 1535.

IPCC (2019) *Special Report on the Ocean and Cryosphere in a Changing Climate* [H.-O. Pörtner, D.C. Roberts, V. Masson-Delmotte, P. Zhai, M. Tignor, E. Poloczanska, K. Mintenbeck, A. Alegría, M. Nicolai, A. Okem, J. Petzold, B. Rama, N.M. Weyer (eds.)].

Jacobi H-W and 8 others (2015) Black carbon in snow in the upper Himalayan Khumbu Valley, Nepal: Observations and modeling of the impact on snow albedo, melting, and radiative forcing. *The Cryosphere* **9**(4), 1685–1699. doi: 10.5194/tc-9-1685-2015

Jia R, Liu Y, Chen B, Zhang Z and Huang J (2015) Source and transportation of summer dust over the Tibetan Plateau. *Atmospheric Environment* **123**, 210–219. doi: 10.1016/j.atmosenv.2015.10.038

Jouzel J, Merlivat L and Lorius C (1982) Deuterium excess in an East Antarctic ice core suggests higher relative humidity at the oceanic surface during the last glacial maximum. *Nature* **299**(5885), 688–691. doi: 10.1038/299688a0

Juhlke TR and 7 others (2019) Assessing moisture sources of precipitation in the Western Pamir Mountains (Tajikistan, Central Asia) using deuterium excess. *Tellus B: Chemical and Physical Meteorology* **71**(1), 1601987. doi: 10.1080/16000889.2019.1601987

Kaspari SD and 6 others (2011) Recent increase in black carbon concentrations from a Mt. Everest ice core spanning 1860-2000 AD: Mt. Everest ice core black carbon. *Geophysical Research Letters* **38**(4). doi: 10.1029/2010GL046096

Kaspari SD, Painter TH, Gysel M, Skiles SM and Schwikowski M (2014) Seasonal and elevational variations of black carbon and dust in snow and ice in the Solu-Khumbu, Nepal and estimated radiative forcings. *Atmospheric Chemistry and Physics* **14**(15), 8089–8103. doi: 10.5194/acp-14-8089-2014

Konishchev VN, Golubev VN and Sokratov SA (2003) Sublimation from a seasonal snow cover and an isotopic content of ice wedges in the light of a paleoclimate reconstructions, 8th Int. Conference on Permafrost, Lisse, Swets and Zeitlinger, Zurich, 585–590.

Lee YH and 25 others (2013) Evaluation of preindustrial to present-day black carbon and its albedo forcing from Atmospheric Chemistry and Climate Model Intercomparison Project (ACCMIP). *Atmospheric Chemistry and Physics* **13**(5), 2607–2634. doi: 10.5194/acp-13-2607-2013

Li X and 13 others (2018) Light-absorbing impurities in a southern Tibetan Plateau glacier: Variations and potential impact on snow albedo and

radiative forcing. *Atmospheric Research* **200**, 77–87. doi: 10.1016/j.atmosres.2017.10.002

Liu Q and 7 others (2015) A study of longitudinal and altitudinal variations in surface water stable isotopes in West Pamir, Tajikistan. *Atmospheric Research* **153**, 10–18. doi: 10.1016/j.atmosres.2014.07.029

Lu Z, Streets DG, Zhang Q and Wang S (2012) A novel back-trajectory analysis of the origin of black carbon transported to the Himalayas and Tibetan Plateau during 1996–2010. *Geophysical Research Letters* **39**(1), 2011GL049903. doi: 10.1029/2011GL049903

Lund J and 6 others (2020) Mapping snowmelt progression in the upper Indus basin with synthetic aperture radar. *Frontiers in Earth Science* **7**, 318. doi: 10.3389/feart.2019.00318

Mayer C and 6 others (2014) Accumulation studies at a high elevation glacier site in central Karakorum. *Advances in Meteorology*, 1–12. doi: 10.1155/2014/215162

Mayer C, Lambrecht A, Beló M, Smiraglia C and Diolaiuti G (2006) Glaciological characteristics of the ablation zone of Baltoro glacier, Karakoram, Pakistan. *Annals of Glaciology* **43**, 123–131. doi: 10.3189/172756406781812087

Ménégoz M and 11 others (2014) Snow cover sensitivity to black carbon deposition in the Himalayas: From atmospheric and ice core measurements to regional climate simulations. *Atmospheric Chemistry and Physics* **14**(8), 4237–4249. doi: 10.5194/acp-14-4237-2014

Ming J and 6 others (2009) Black carbon (BC) in the snow of glaciers in west China and its potential effects on albedos. *Atmospheric Research* **92**(1), 114–123. doi: 10.1016/j.atmosres.2008.09.007

Ming J, Xiao C, Wang F, Li Z and Li Y (2016) Grey Tienshan Urumqi Glacier No.1 and light-absorbing impurities. *Environmental Science and Pollution Research* **23**(10), 9549–9558. doi: 10.1007/s11356-016-6182-7

Mori T and 6 others (2016) Improved technique for measuring the size distribution of black carbon particles in liquid water. *Aerosol Science and Technology* **50**(3), 242–254. doi: 10.1080/02786826.2016.1147644

Mukhopadhyay B, Khan A and Gautam R (2015) Rising and falling river flows: Contrasting signals of climate change and glacier mass balance from the eastern and western Karakoram. *Hydrological Sciences Journal* **60**(12), 2062–2085. doi: 10.1080/02626667.2014.947291

National Research Council (2012) *Climate Change: Evidence, Impacts, and Choices: PDF Booklet*. Washington, DC: The National Academies Press.

National Weather Forecasting Centre (2019) Monthly Weather Report, February, 2019. Pakistan Meteorological Department.

Nischal AR and Hunt KMR (2022) Evaluating winter precipitation over the Western Himalayas in a high-resolution Indian regional reanalysis using multisource climate datasets. *Journal of Applied Meteorology and Climatology* **61**(11), 1613–1633. doi: 10.1175/JAMC-D-21-0172.1

NOAA (2023a) Clustering equations. https://www.ready.noaa.gov/documents/Tutorial/html/traj_cluseqn.html (accessed 29 July 2024).

NOAA (2023b) HYSPLIT User's Guide: Trajectory/Run cluster analysis. https://www.arl.noaa.gov/documents/reports/hysplit_user_guide.pdf (accessed 29 July 2024).

Pfahl S and Sodemann H (2014) What controls deuterium excess in global precipitation? *Climate of the Past* **10**(2), 771–781. doi: 10.5194/cp-10-771-2014

Pritchard DMW, Forsythe N, Fowler HJ, O'Donnell GM and Li XF (2019) Evaluation of upper Indus near-surface climate representation by WRF in the high Asia refined analysis. *Journal of Hydrometeorology* **20**(3), 467–487. doi: 10.1175/JHM-D-18-0030.1

Qu B and 8 others (2014) The decreasing albedo of the Zhadang glacier on western Nyainqentanglha and the role of light-absorbing impurities. *Atmospheric Chemistry and Physics* **14**(20), 11117–11128. doi: 10.5194/acp-14-11117-2014

Ramanathan V and Carmichael G (2008) Global and regional climate changes due to black carbon. *Nature Geoscience* **1**(4), 221–227. doi: 10.1038/ngeo156

Rindsberger M, Magaritz M, Carmi I and Gilad D (1983) The relation between air mass trajectories and the water isotope composition of rain in the Mediterranean Sea area. *Geophysical Research Letters* **10**(1), 43–46. doi: 10.1029/GL010i001p00043

Rodhe H, Persson C and Åkesson O (1972) An investigation into regional transport of soot and sulfate aerosols. *Atmospheric Environment* **6**(9), 675–693. doi: 10.1016/0004-6981(72)90025-X

Rolph G, Stein A and Stunder B (2017) Real-time Environmental Applications and Display sYstem: READY. *Environmental Modelling and Software* **95**, 210–228. doi: 10.1016/j.envsoft.2017.06.025

Seligman G (1936) *Snow Structure and Ski Fields: Being an Account of Snow and Ice Forms Met with in Nature, and a Study on Avalanches and Snowcraft*. London: MacMillan.

Sharma B and 12 others (2010) The Indus and the Ganges: River basins under extreme pressure. *Water International* **35**(5), 493–521. doi: 10.1080/02508060.2010.512996

Shrestha M and 6 others (2015) Integrated simulation of snow and glacier melt in water and energy balance-based, distributed hydrological modeling framework at Hunza River Basin of Pakistan Karakoram region: Integrated snow and glaciermelt model. *Journal of Geophysical Research: Atmospheres* **120**(10), 4889–4919. doi: 10.1002/2014JD022666

Sinclair KE and Marshall SJ (2009) Temperature and vapour-trajectory controls on the stable-isotope signal in Canadian Rocky Mountain snowpacks. *Journal of Glaciology* **55**(191), 485–498. doi: 10.3189/002214309788816687

Spangenberg JE (2012) Caution on the storage of waters and aqueous solutions in plastic containers for hydrogen and oxygen stable isotope analysis. *Rapid Communications in Mass Spectrometry* **26**(22), 2627–2636. doi: 10.1002/rcm.6386

Spangenberg JE and Vennemann TW (2008) The stable hydrogen and oxygen isotope variation of water stored in polyethylene terephthalate (PET) bottles. *Rapid Communications in Mass Spectrometry* **22**(5), 672–676. doi: 10.1002/rcm.3415

Stein AF, Draxler RR, Rolph GD, Stunder BJB, Cohen MD and Ngan F (2015) NOAA's HYSPLIT atmospheric transport and dispersion modeling system. *Bulletin of the American Meteorological Society* **96**(12), 2059–2077. doi: 10.1175/BAMS-D-14-00110.1

Sterle KM, McConnell JR, Dozier J, Edwards R and Flanner MG (2013) Retention and radiative forcing of black carbon in eastern Sierra Nevada snow. *The Cryosphere* **7**(1), 365–374. doi: 10.5194/tc-7-365-2013

Svensson J and17 others (2018) Light-absorption of dust and elemental carbon in snow in the Indian Himalayas and the Finnish Arctic. *Atmospheric Measurement Techniques* **11**(3), 1403–1416. doi: 10.5194/amt-11-1403-2018

Thakur RC and 6 others (2021) Multi-layer distribution of Black Carbon and inorganic ions in the snowpacks of western Himalayas and snow albedo forcing. *Atmospheric Environment* **261**, 118564. doi: 10.1016/j.atmosenv.2021.118564

Thind PS, Chandel KK, Sharma SK, Mandal TK and John S (2019) Light-absorbing impurities in snow of the Indian Western Himalayas: Impact on snow albedo, radiative forcing, and enhanced melting. *Environmental Science and Pollution Research* **26**(8), 7566–7578. doi: 10.1007/s11356-019-04183-5

Uemura R, Matsui Y, Motoyama H and Yoshida N (2007) Deuterium and oxygen-18 determination of microliter quantities of a water sample using an automated equilibrator. *Rapid Communications in Mass Spectrometry* **21**(11), 1783–1790. doi: 10.1002/rcm.3022

Wake CP (1989) Glaciochemical investigations as a tool for determining the spatial and seasonal variation of snow accumulation in the Central Karakoram, Northern Pakistan. *Annals of Glaciology* **13**, 279–284. doi: 10.3189/S0260305500008053

Warren SG (1982) Optical properties of snow. *Reviews of Geophysics* **20**(1), 67–89. doi: 10.1029/RG020i001p00067

Wiscombe WJ and Warren SG (1980) A model for the spectral albedo of snow. I: Pure snow. *Journal of the Atmospheric Sciences* **37**(12), 2712–2733. doi: 10.1175/1520-0469(1980)037<2712:AMFTSA>2.0.CO;2

World Economic Forum (2016) The Global Risks Report 2016 11th Edition. http://www3.weforum:docs/GRR/WEF_GRR16.pdf (accessed April 2023)

Xing Y and 12 others (2024) Dust storms from the Taklamakan Desert significantly darken snow surface on surrounding mountains. *Atmospheric Chemistry and Physics* **24**(9), 5199–5219. doi: 10.5194/acp-24-5199-2024

Xu B and 11 others (2009a) Black soot and the survival of Tibetan glaciers. *Proceedings of the National Academy of Sciences* **106**(52), 22114–22118. doi: 10.1073/pnas.0910444106

Xu B and 7 others (2009b) Deposition of anthropogenic aerosols in a southeastern Tibetan glacier. *Journal of Geophysical Research* **114**(D17), D17209. doi: 10.1029/2008JD011510

Xu B, Cao J, Joswiak DR, Liu X, Zhao H and He J (2012) Post-depositional enrichment of black soot in snow-pack and accelerated melting of Tibetan glaciers. *Environmental Research Letters* **7**(1), 014022. doi: 10.1088/1748-9326/7/1/014022

Xu B, Yao T, Liu X and Wang N (2006) Elemental and organic carbon measurements with a two-step heating-gas chromatography system in snow samples from the Tibetan Plateau. *Annals of Glaciology* **43**, 257–262. doi: 10.3189/172756406781812122

Yang S, Xu B, Cao J, Zender CS and Wang M (2015) Climate effect of black carbon aerosol in a Tibetan Plateau glacier. *Atmospheric Environment* **111**, 71–78. doi: 10.1016/j.atmosenv.2015.03.016

Yi Y, Liu S, Zhu Y, Wu K, Xie F and Saifullah M (2021) Spatiotemporal heterogeneity of snow cover in the central and western Karakoram Mountains based on a refined MODIS product during 2002–2018. *Atmospheric Research* **250**, 105402. doi: 10.1016/j.atmosres.2020.105402

Young GJ and Hewitt K (1990) Hydrology research in the upper Indus Basin, Karakoram Himalaya, Pakistan. *Hydrology of Mountainous Areas* (Proceedings of the Strbské Pleso Workshop, Czechoslovakia **1990**, 139–152.

Yu W and 6 others (2013) *Indus Basin of Pakistan: Impacts of Climate Risks on Water and Agriculture. Directions in Development; Countries and Regions*. Washington, DC: World Bank.

Yuan T and 9 others (2019) Influence of dynamic and thermal forcing on the meridional transport of Taklimakan Desert dust in spring and summer. *Journal of Climate* **32**(3), 749–767. doi: 10.1175/JCLI-D-18-0361.1

Zemp M and 14 others (2019) Global glacier mass changes and their contributions to sea-level rise from 1961 to 2016. *Nature* **568**(7752), 382–386. doi: 10.1038/s41586-019-1071-0

Zhang Y and 13 others (2017) Characteristics of black carbon in snow from Laohugou No. 12 glacier on the northern Tibetan Plateau. *Science of the Total Environment* **607–608**, 1237–1249. doi: 10.1016/j.scitotenv.2017.07.100

Zhang YL, Kang SC, Gao TG, Sprenger M, Zhang W and Wang ZQ (2023) Black carbon size in snow of Chinese Altai Mountain in Central Asia. *Advances in Atmospheric Sciences* **40**(7), 1199–1211. doi: 10.1007/s00376-022-2141-z